



A lightweight X-type metallic lattice in single-phase forced convection



H.B. Yan^{a,b}, Q.C. Zhang^{b,c}, T.J. Lu^{b,c,*}, T. Kim^{d,*}

^a School of Energy and Power Engineering, Xi'an Jiaotong University, Xi'an 710049, PR China

^b Multidisciplinary Research Center for Lightweight Structures and Materials, Xi'an Jiaotong University, Xi'an 710049, PR China

^c State Key Laboratory for Strength and Vibration of Mechanical Structures, Xi'an Jiaotong University, Xi'an 710049, PR China

^d School of Mechanical Engineering, University of the Witwatersrand, Johannesburg, Wits 2050, South Africa

ARTICLE INFO

Article history:

Received 29 April 2014

Received in revised form 13 November 2014

Accepted 18 November 2014

Available online 19 December 2014

Keywords:

Forced convection

X-type lattice

Heat transfer enhancement

Spiral primary flow

Secondary flow

ABSTRACT

The superior capability of bearing thermal and mechanical loads to other types of open cellular materials has led to advances in developing new periodic cellular materials. We introduce a lightweight X-type lattice fabricated via the metal sheet folding and present its thermo-fluidic characteristics in single-phase forced convection. For fixed porosity, thermal conductivity and Reynolds number, the X-type lattice provides overall heat removal capacity up to two times higher than reference periodic cellular materials. The unique morphology of the X-type lattice results in a large scale spiral primary flow, which interacts with several secondary flows. These fluid flow behaviors and the induced complex flow mixing substantially enhance heat transfer on both the substrate and ligaments. However, the X-type lattice causes roughly three times higher pressure drop than reference periodic cellular materials for a given Reynolds number. Overall, superior heat transfer is achieved by the X-type lattice for a fixed pumping power.

© 2014 Elsevier Ltd. All rights reserved.

1. Introduction

In thermal management systems, a variety of heat dissipation media have been used. The spectrum of such media includes simple two dimensional prismatic media (e.g., pin-fins [1]), stochastic cellular media (e.g., metal foams [2]) and periodic cellular media (e.g., wire-screens [3], lattice-frame materials [4] and Kagome lattices [5]). Amongst them, cellular metals including open-cell metal foams and periodic cellular materials (PCMs) are promising for multifunctional applications where simultaneous thermal and mechanical load bearing capability is required [6–10]. In particular, PCMs (Fig. 1) provide better specific strength and stiffness than stochastic ones [11]. Consequently, considerable efforts have been devoted to developing mechanically and thermally effective PCMs.

With rapid advances in manufacturing technology, different methods have been introduced to fabricate more design friendly and controllable PCMs, such as metal wire weaving [12], investment casting [13], cylinder assembling [14], and metal sheet folding [15]. In particular, metal sheet folding is considered simpler and more cost-effective [11]. Using this method, PCMs having

various cell topologies (e.g., tetrahedron and pyramid) can be fabricated [11]. To fabricate a tetrahedral lattice core for sandwich construction, the perforation of a complete metal sheet to form perforated hexagonal holes is required [15], wasting a considerable amount of material. In contrast, to fabricate a pyramidal lattice (Fig. 2(a)), an alternative yet more cost-effective method of slitting and expanding a complete metal sheet has been developed to form the required diamond holes, allowing much more material to be utilized [16]. Further, half pitch shifting of the metal sheet with diamond holes has been found to form a new periodic lattice with ligaments intersecting into an “X shape,” the so-called “X-type lattice;” see Fig. 2(b). Mechanically, relative to pyramidal lattice, it has been demonstrated that the X-type lattice provides approximately 30% higher peak compressive and shear strengths for a given relative density [17,18].

Morphologically, whilst LFM, Kagome and WBK lattices typically have circular ligaments (see Fig. 1); the ligaments of an X-type lattice have a rectangular cross-section (Fig. 2). Further, by changing relevant parameters of the metal sheet and moulds, the method of metal sheet folding provides more design flexibility. For a given porosity, for example, an X-type lattice having more frontal area can be easily fabricated by using a thinner metal sheet with smaller diamond holes, providing thus better heat transfer [9,19]. In comparison, for PCMs with circular cross-sectioned ligaments (Fig. 1), the variation of frontal area is always accompanied by varying porosity due to changing ligament diameter.

* Corresponding authors at: State Key Laboratory for Strength and Vibration of Mechanical Structures, Xi'an Jiaotong University, Xi'an 710049, PR China (T.J. Lu). Tel.: +86 029 82665937.

E-mail addresses: tjlu@mail.xjtu.edu.cn (T.J. Lu), tongkim@wits.ac.za (T. Kim).

Nomenclature

A	surface area (m^2)
b_1, b_2	widths of the intersection point in Fig. 4 (m)
c_p	specific heat of fluid ($\text{J}/(\text{kgK})$)
C	empirical constant in Eq. (9)
C_p	pressure coefficient defined in Eq. (8)
f_H	friction factor defined in Eq. (7)
h	local heat transfer coefficient ($\text{W}/(\text{m}^2\text{K})$)
H	X-type lattice core height (m)
k_f	thermal conductivity of fluid ($\text{W}/(\text{mK})$)
k_s	thermal conductivity of solid ($\text{W}/(\text{mK})$)
l	length of a core unit cell (m)
l_1	geometric parameter defined in Eq. (A.6) (m)
L	length of the sandwich panel (m)
n	empirical constant in Eq. (9)
Nu	local Nusselt number
Nu_H	area-averaged Nusselt number
p	static pressure in Eq. (8) (Pa)
q''	heat flux (W/m^2)
r_1-r_3	fillet radii shown in Fig. 4 (m)
Re_H	Reynolds number defined in Eq. (2)
t	thickness of a substrate (m)
t_l	thickness of a core ligament (m)
T_f	bulk mean fluid temperature in Eq. (5) (K)
T_{in}	inlet fluid temperature (K)

T_w	wall temperature (K)
U_c	inlet centerline velocity (m/s)
U_m	mean inlet velocity (m/s)
V_m	velocity magnitude (m/s)
w	width of a core unit cell (m)
w_l	width of a core ligament (m)
W	width of a sandwich panel (m)
x, y, z	Cartesian coordinates (m)
y^*	dimensionless wall distance

Greek symbols

α, β	included angles shown in Fig. 4 ($^\circ$)
Δp	pressure drop (Pa)
ε	porosity
μ	dynamic viscosity of fluid (Pa s)
ρ	density of fluid (kg/m^3)
ρ_{SA}	surface area density (m^2/m^3)

Abbreviations

OA	orientation A
OB	orientation B
PCM	periodic cellular material

This study aims to investigate single phase forced convective heat transfer in an X-type lattice, and compare its performance with other types of PCMs. A series of experiments and numerical simulations are conducted to gain physical insight into its overall and detailed thermo-fluidic characteristics. Particular focus is placed upon revealing the distinctive forced convective flow features associated with the unique morphology of the X-type lattice and their effects on local and overall heat transfer.

2. Experimental details

2.1. Test apparatus

With reference to Fig. 3, the test rig consists of an air supply system, a test section and a data acquisition system. Air at ambient conditions is drawn into a rectangular channel by a centrifugal fan. The test channel, having width W and height H , is made from low-conducting acrylic plates. Before the test sample, a

honeycomb is inserted in a long parallel passage having length $48H$ (not shown in Fig. 3). The sample, a sandwich panel with X-type lattice core, is inserted in the test section with the inner surfaces of the substrates flush with the channel inner surfaces.

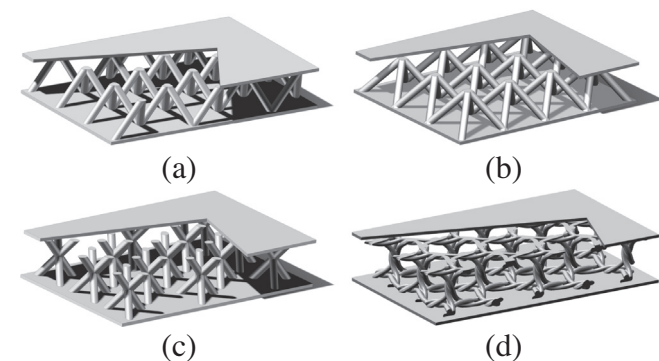


Fig. 1. Sandwich panels with (a) tetrahedral core (also called “lattice-frame material” (LFM)), (b) pyramidal core, (c) Kagome core and (d) wire-woven bulk Kagome (WBK) core.

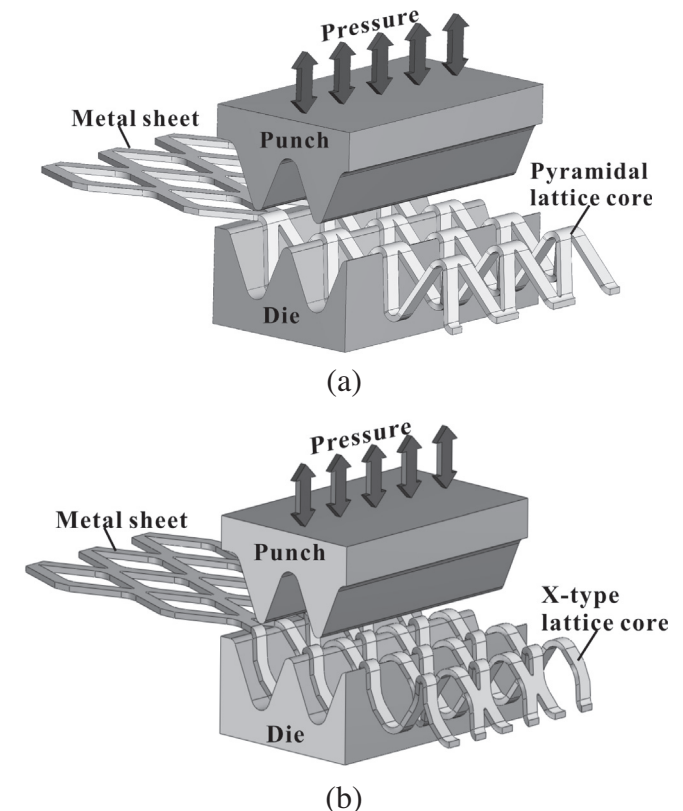


Fig. 2. Fabrication of (a) pyramidal and (b) X-type lattice by metal sheet folding.

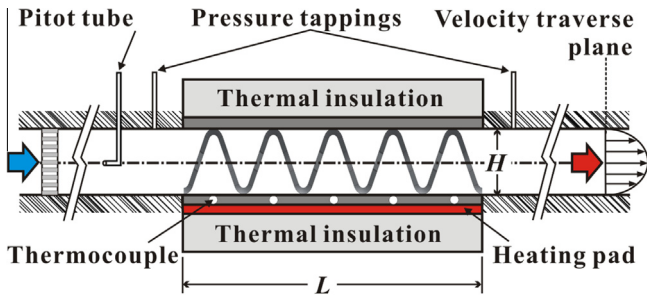
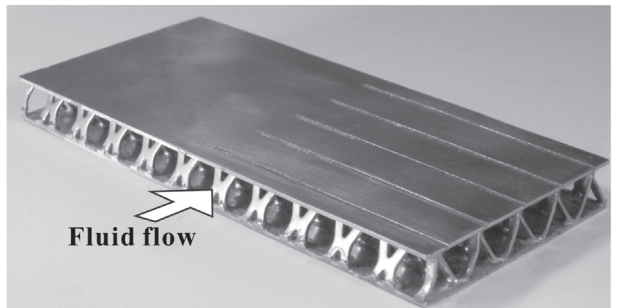


Fig. 3. Schematic of a test section for pressure drop and heat transfer measurements.

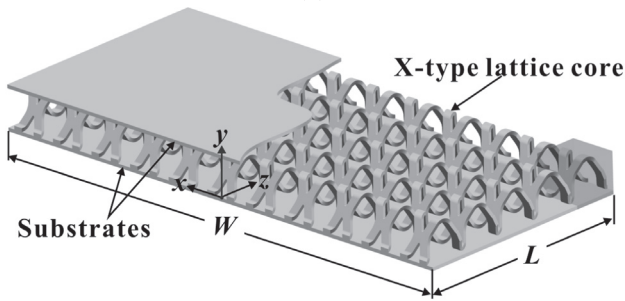
2.2. Test sample

The sandwich panel used in pressure drop and heat transfer experiments is shown in Fig. 4(a), which has not yet been optimized. The X-type lattice core is fabricated by periodically folding a perforated sheet made of AISI 304 stainless steel, with $k_s = 16.2 \text{ W/(mK)}$ [20]. The X-type lattice is then brazed onto AISI 304 stainless steel substrates (face-sheets) with Ni–25.0Cr–10.0P brazing filler in a vacuum furnace. Detailed fabrication processes and procedures are documented in [17].

The X-type lattice sandwich panel has overall dimensions W and L , accommodating eleven unit cells in the transverse direction



(a)



(b)

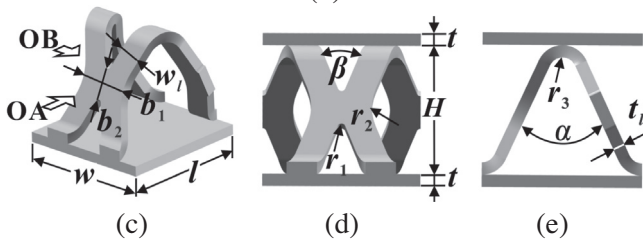


Fig. 4. Details of X-type lattice sandwich panel: (a) as-fabricated sample; (b) three-dimensional representation of X-type lattice core; (c) unit cell; (d) frontal view of unit cell along z-axis (Orientation A, OA); (e) frontal view of unit cell along x-axis (Orientation B, OB).

(along the x -axis) to minimize sidewall effects; see Fig. 4(b). A unit cell of the X-type lattice and the corresponding frontal views in two mutually perpendicular orientations are shown in Fig. 4(c–e). The morphology of the unit cell depends on nine independent dimensions, i.e., $l, w, H, w_1, t_1, r_1, r_2, \alpha$ and β . Corresponding morphological parameters, i.e., b_1, b_2, r_3 , porosity (ϵ) and surface area density (ρ_{SA}), can subsequently be calculated from the formulae given in Appendix A. Table 1 summarizes the geometric parameters of the test sample.

2.3. Endwall flow visualization

To visualize endwall flow pattern, an additional X-type lattice sandwich panel with transparent substrates is fabricated. The X-type lattice is attached to Perspex plates by a transparent UV adhesive, with the brazed joints well represented by the bonding joints. An oil–dye mixture technique is used to visualize the flow pattern on the lower endwall surface. The surfaces of the upper endwall plate and the lattice core are painted in black to offer a background. The surface flow pattern can be visualized when aerodynamic shear stress redistributes the mixture (fluorescent powder and light diesel fuel). Ultraviolet light is used to illuminate the flow pattern while photographing.

2.4. Velocity and pressure drop measurements

To quantify the mass flow rate of convective flow in the X-type lattice sandwich panel, the velocity profile at the exit of a long parallel flow channel ($50H$ in length) placed downstream the test sample is traversed along channel height (the y -axis); see Fig. 3. Mean velocity over the channel height (U_m) is calculated by integrating the measured velocity profile and correlated with the measured inlet centerline velocity (U_c) by a Pitot tube, as:

$$U_m = 0.8283U_c - 0.3429 \tag{1}$$

During the present measurements, the mean velocity is set to vary from 2.7 m/s to 12.6 m/s.

Two additional static pressure tapings are installed on the upper endwall (6 mm upstream and downstream the test sample, respectively) to measure pressure drop during heat transfer measurements.

2.5. Heat transfer measurement

Constant heat flux is imposed on the bottom substrate of the sandwich panel by a film heating element connected to a DC power supply. To measure endwall temperature, five T-type bead thermocouples (0.4 mm in diameter) are embedded in grooves (0.5 mm in depth) machined on the outer surface of the bottom substrate (Fig. 3). Each thermocouple is located at the center of each of the five unit cells distributed along the z -axis. A thermal adhesive (Arctic Silver™) is used to fill the gap between the heating element and the substrate. The test section is covered by a low-conducting foam to minimize heat loss.

Table 1
Geometric parameters of the test sample.

Parameter	Value	Parameter	Value
b_1	0.00462 m	t_1	0.00091 m
b_2	0.0027 m	w	0.012 m
H	0.00966 m	w_1	0.00216 m
l	0.012 m	W	0.132 m
L	0.060 m	α	50°
r_1	0.0003 m	β	42°
r_2	0.0043 m	ϵ	0.932
r_3	0.00105 m	ρ_{SA}	205 m ² /m ³
t	0.0009 m		

Two additional T-type bead thermocouples are installed upstream and downstream the test section to measure inlet and outlet coolant temperatures. All the measurements are conducted under steady-state conditions.

2.6. Data reduction and uncertainty analysis

In this study, the channel height (H) is selected as a characteristic length to facilitate comparison with existing data for other PCMs, e.g., LFM and Kagome. Consequently, the Reynolds number (Re_H) is defined as:

$$Re_H = \frac{\rho U_m H}{\mu} \quad (2)$$

where ρ and μ are the density and dynamic viscosity of air, respectively.

For heat transfer characterization, the measured local heat transfer coefficient, $h(0,0,z)$, and Nusselt number, $Nu(0,0,z)$, along the z -axis are defined as:

$$h(0,0,z) = \frac{q''}{T_w(0,0,z) - T_f(z)} \quad (3)$$

$$Nu(0,0,z) = \frac{h(0,0,z)H}{k_f} \quad (4)$$

where q'' is the heat flux imposed by the heating element, $T_w(0,0,z)$ is the substrate temperature measured by the thermocouples, and k_f is the thermal conductivity of air. $T_f(z)$ refers to the local bulk mean fluid temperature calculated from energy balance, as:

$$T_f(z) = T_{in} + \frac{zq''}{\rho U_m H c_p} \quad (5)$$

where T_{in} is the measured inlet air temperature and c_p is the specific heat of air. Subsequently, the area-averaged Nusselt number, Nu_H , is estimated as:

$$Nu_H = \frac{1}{L} \sum_1^5 \left[Nu(0,0,z) \frac{L}{5} \right] \quad (6)$$

which is used to evaluate the overall heat transfer performance of the present X-type lattice sandwich panel.

For pressure drop evaluation, a dimensionless friction factor (f_H) is defined as:

$$f_H = \frac{\Delta p}{L} \frac{H}{\rho U_m^2 / 2} \quad (7)$$

where Δp denotes the pressure drop measured by inlet and outlet pressure tapings.

An uncertainty analysis is performed following the root mean square method reported by Coleman and Steele [21]. The density and viscosity of air are derived based on inlet static pressure and temperature; and therefore, their uncertainties are neglected. Static pressure is measured by a DSA 3217 differential pressure transducer (Scanivalve™) with a resolution of 0.3 Pa. Consequently, the uncertainties associated with the Reynolds number and friction factor are estimated to be within 3.1% and 6.2%, respectively.

Heat loss through the channel walls is estimated by performing energy balance based on heat input and measured inlet and outlet air temperatures, and is found to be less than 4%. Temperature from T-type thermocouples (Omega™) with an uncertainty of 0.1 K is recorded by an Agilent 34970A data logger. The thermal conductivity of air is evaluated at the arithmetic mean value of inlet and outlet air temperatures. Its uncertainty is estimated to be less than 1.8% (within the present operating range of 296–309 K). Consequently, the uncertainties for heat transfer coefficient and Nusselt number are estimated to be less than 4.7% and 5.0%, respectively.

3. Numerical simulation

The structural complexity of the X-type lattice limits inevitably experimental access into local thermo-fluidic features which would, however, provide crucial information regarding heat transfer mechanisms within the lattice. For this reason, three-dimensional numerical simulations are performed using a commercial software package, ANSYS14.0.

The X-type lattice core and the substrates are first modeled by the Sheet Metal Tools in SolidWorks™. The fillets (or brazed joints, see Fig. 5) with radius 1 mm are created between the substrates and the core. To improve mesh quality, sharp edges of the fillets are removed in the numerical model as illustrated in Fig. 5(b).

Due to geometrical symmetry of the X-type lattice, only five half unit cells along the streamwise direction are considered, as shown in Fig. 6(a). Short inlet and outlet channels (both have length H) are included to improve numerical stability. Fully developed isothermal turbulent flow between two parallel plates is firstly simulated and validated by the measured velocity profile (see Section 2.4). For brevity, details are not presented here. The simulated flow field and constant fluid temperature are used as the inlet boundary condition in Fig. 6(a). Symmetric boundary conditions are applied upon the symmetric faces. An outlet boundary condition specifying the mass conservation is used at the outlet of the computational domain. Uniform heat flux is applied upon the outer surface of the bottom substrate, while other outer surfaces of the computational domain are set to be adiabatic.

A hybrid mesh incorporating both tetrahedron and prism elements are adopted to discretize solid and fluid domains; see Fig. 6(b). Fine mesh with ten layers of prism elements is generated in the fluid domain near the walls to resolve boundary layers, while coarse mesh is generated in other regions. Non-conformal interfaces are adopted to couple the fluid and solid domains.

The problem of incompressible steady-state flow and conjugated heat transfer is solved using the double precision solver ANSYS CFX 14.0 based on the finite volume method. The shear stress transport (SST) turbulence model [22] incorporating a dimensionless wall distance (y^+) less than 1.0 is adopted for internal turbulent flow due to its improved capability in predicting large flow separation [23] that is expected to occur in the X-type lattice. High resolution scheme is selected to discretize the advection terms in the governing equations to reduce numerical error. The solution is thought to be converged when the normalized residuals of all the governing equations are less than 10^{-6} .

To check mesh sensitivity, three different meshes with 4,069,119, 6,462,252 and 9,430,376 elements are employed. Table 2 compares the predicted flow and heat transfer parameters at the highest Reynolds number (i.e., $Re_H = 5700$) considered in the present simulations. In Table 2, the friction factor and Nusselt number are calculated according to Eqs. (3)–(7), whilst the pressure coefficient (C_p) is defined as:

$$C_p(x,y,z) = \frac{p(x,y,z) - p(0,H,-0.1L)}{\rho U_m^2 / 2} \quad (8)$$

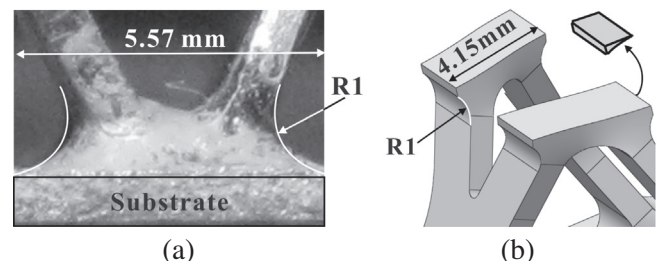


Fig. 5. Simplification of brazed joint: (a) actual joint; (b) numerically modeled joint.

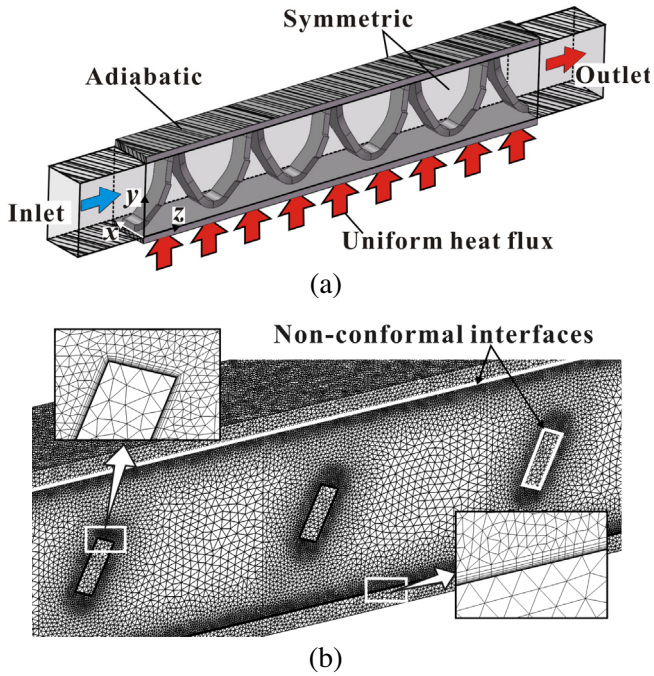


Fig. 6. Details of numerical simulation: (a) schematic illustration of computational domain and boundary conditions; (b) representative mesh.

Table 2
Predicted flow and heat transfer parameters with three different meshes at $Re_H = 5700$.

Total elements	4,069,119	6,462,252	9,430,376
$C_p(0, H, 0.1L)$	-3.8859	-3.9726	-3.9628
$C_p(0, H, 0.3L)$	-6.5426	-6.6797	-6.6080
$C_p(0, H, 0.5L)$	-10.251	-10.787	-10.824
$C_p(0, H, 0.7L)$	-13.621	-14.024	-14.130
$C_p(0, H, 0.9L)$	-16.774	-17.471	-17.481
f_H	2.8392	2.9509	2.9495
$Nu(0, 0, 0.1L)$	135.5	134.7	135.9
$Nu(0, 0, 0.3L)$	135.9	138.3	139.7
$Nu(0, 0, 0.5L)$	142.1	143.2	144.7
$Nu(0, 0, 0.7L)$	147.1	147.1	149.6
$Nu(0, 0, 0.9L)$	150.3	150.5	153.2
Nu_H	142.2	142.8	144.6

where $p(x, y, z)$ is the static pressure at an arbitrary position. All the predicted values from the last two meshes exhibit a deviation less than 1.7%. Therefore, the mesh with 6,462,252 elements is used in all subsequent simulations. Detailed validation of the numerical model is presented in Section 4.

4. Discussion of results

4.1. Enhanced overall heat transfer

The heat dissipation capability of the X-type lattice is first discussed. As previously mentioned, present X-type lattice core only contains five rows of unit cells in the streamwise direction. To ensure a reliable comparison to other similar PCMs with heat transfer data in approximately fully developed thermal flow reported in the open literature [4,5,24], the entry and exit region effects on overall heat transfer have to be clarified for the X-type lattice sandwich panel. Fig. 7(a) presents streamwise heat transfer distribution at $Re_H = 5700$, where the local Nusselt number is calculated from Eq. (4). Both the experimental and numerical data show that Nusselt number slightly increases from the first to the

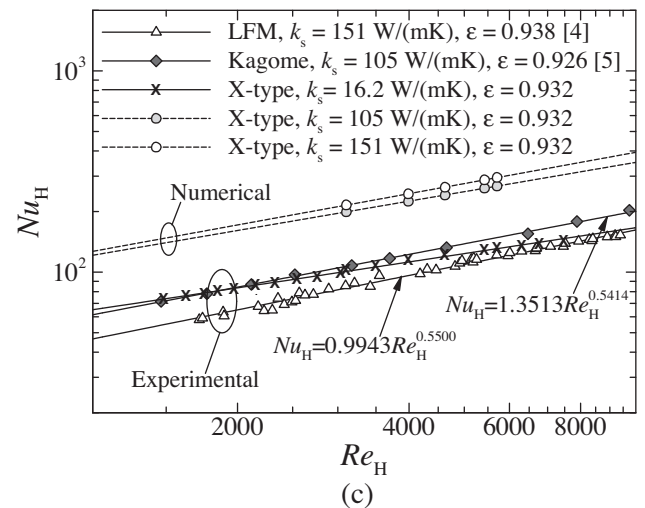
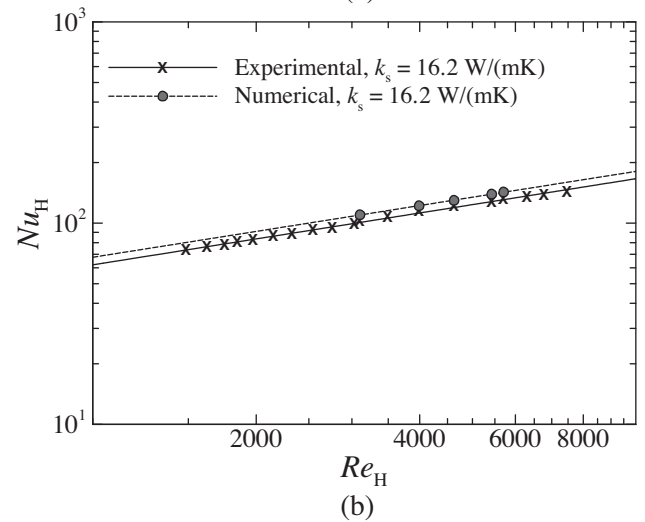
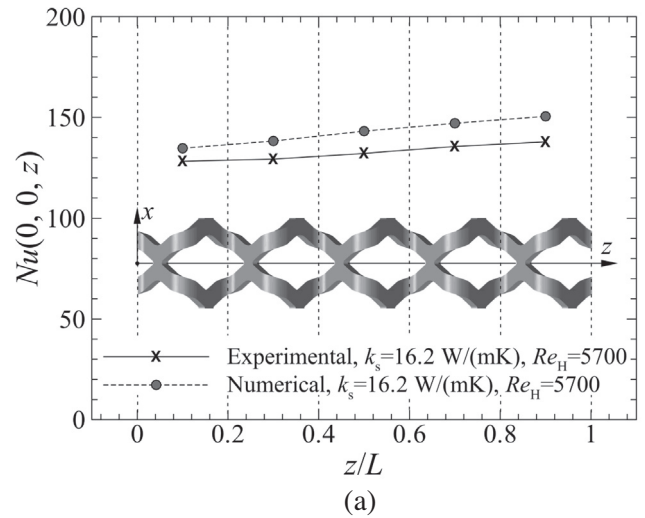


Fig. 7. Overall heat transfer of X-type lattice sandwich panel: (a) streamwise variation of Nusselt number at $Re_H = 5700$; (b) Nu_H versus Re_H for X-type lattice; (c) comparison with LFM [4] and Kagome [5] having similar porosities.

fifth unit cell, which is consistent with the trend observed for LFM [24] and tube banks in cross flow [25]. Consequently, the thermal flow crossing the present X-type lattice is developing. However, the increment is limited, with a 7.5% higher Nusselt number in the fifth unit cell (i.e., at $z/L = 0.9$) than that in the first unit cell (i.e., at $z/L = 0.1$) as revealed by the experimental data. It is

believed that when many unit cells are longitudinally arranged, overall heat transfer of the corresponding sandwich panel will be higher than the present result. Therefore, subsequent comparisons with other PCMs are reliable. Additionally, the numerical result shows reasonable agreement with the experimental data, with a deviation of 5.0–9.1% from the first to the last unit cell.

The overall heat transfer of the X-type lattice sandwich panel is quantified in Fig. 7(b), with the Nusselt number (Nu_H) representing the area-averaged value obtained from Eqs. (3)–(6). The measured Nusselt number is correlated as a function of the Reynolds number, as:

$$Nu_H = CRe_H^n \quad (9)$$

where $C = 3.228$ and $n = 0.428$. It should be noted that this correlation is only applicable to the present test sample. Agreement between the two data sets obtained numerically and experimentally is within 8.5%.

Fig. 7(c) compares the area-averaged Nusselt number of the X-type lattice with those of other PCMs at a similar porosity level. Although the present X-type lattice is made of a relatively low-conducting metal ($k_s = 16.2 \text{ W/(mK)}$), it thermally behaves in a similar manner to LFM ($k_s = 151 \text{ W/(mK)}$) [4] and Kagome ($k_s = 105 \text{ W/(mK)}$) [5] made of materials with much higher thermal conductivities. To better understand the thermal behavior of the X-type lattice made of material having same thermal conductivity as LFM or Kagome, a series of numerical simulations are performed. The numerical results are presented in Fig. 7(c). With the same thermal conductivity, it is seen from Fig. 7(c) that the X-type lattice outperforms both LFM and Kagome in the present Reynolds number range ($1400 < Re_H < 7500$), providing approximately 140–170% and 80–100% more heat removal than LFM and Kagome, respectively.

4.2. Heat transfer enhancement mechanisms

In view of the results shown in Fig. 7, it is of interest to understand why such higher heat dissipation can be achieved by the X-type lattice than other periodic cellular materials such as LFM and Kagome. In this section, detailed mechanisms are explored.

4.2.1. Spiral primary flow and secondary flows

The fluid-through porous core of a sandwich panel modifies the primary flow, enhancing therefore its overall heat transfer compared to an empty channel. Although the primary flow patterns are strongly dependent on specific core morphologies, they are largely parallel to the substrates in most PCM-cored sandwich panels [26]. However, it has been found that the X-type lattice induces a large scale spiral primary flow as highlighted by the streamlines in Fig. 8(a), where V_m denotes the magnitude of flow velocity. To elaborate this primary flow pattern, three transverse (x - y) planes in half of the third unit cell (see Fig. 6(a)) are selected. As shown in Fig. 8(b), the velocity vectors on these planes clearly signify the formation of spiral primary flow. At the center of each plane, the velocity magnitude of the primary flow is low. However, a strong tangential flow motion is predominant at the periphery of each plane, demonstrating a counter-clock-wise rotation (viewed from the upstream). Such a tangential flow motion undoubtedly intensifies transverse flow mixing (in the x - y plane).

In addition to forming large scale spiral primary flow, the X-type lattice mainly induces three types of secondary flows, denoted as (A–C) in Fig. 9. Secondary flows (A) and (B) are two cross flows through two types of flow areas denoted as (A) and (B), respectively. Under the influence of spiral primary flow, both of the secondary flows become skewed towards the positive y -axis. Also, it has been found that two counter-rotating vortices take place

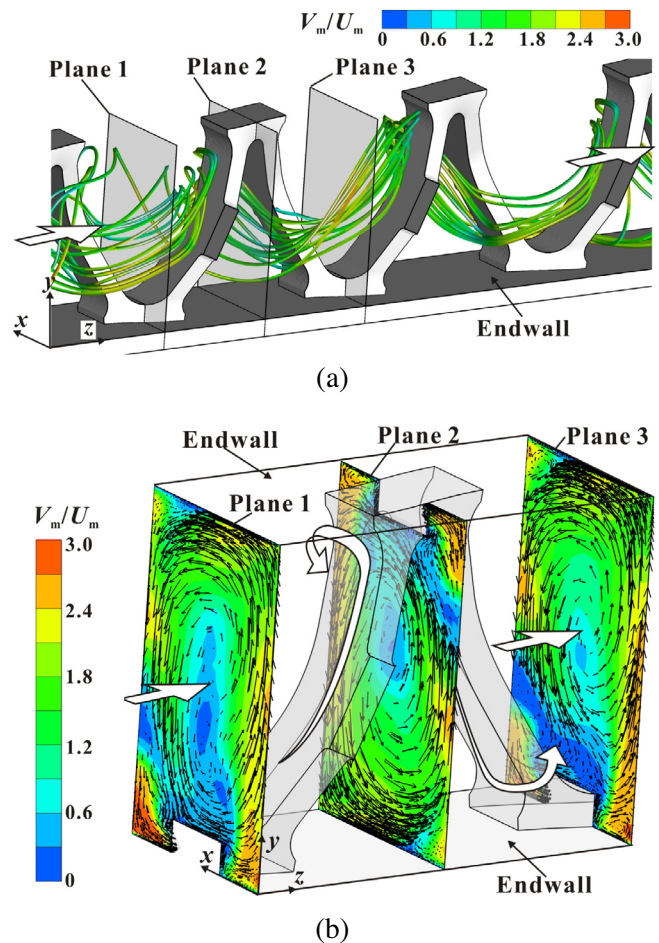


Fig. 8. Spiral primary flow induced by X-type lattice (V_m is velocity magnitude): (a) streamlines highlighting a large scale spiral primary flow through an array of half unit cells; (b) velocity vectors and contours in selected transverse (x - y) planes in half of third unit cell (see Fig. 6(a)).

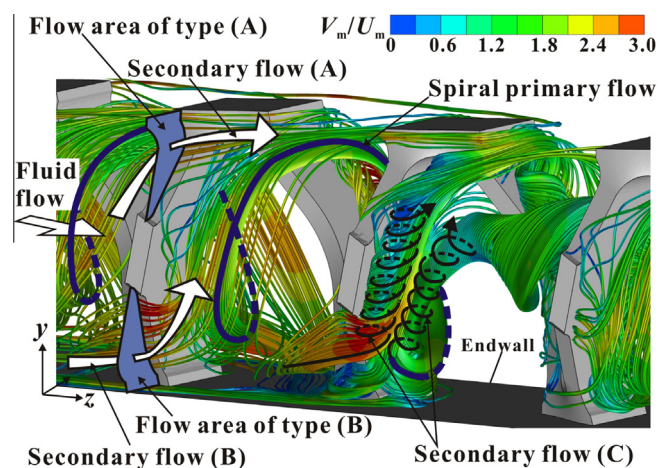


Fig. 9. Secondary flow structures induced by X-type lattice as indicated by streamlines from numerical simulations.

behind every ligament, such as the secondary flow (C) highlighted in Fig. 9. After passing flow area of type (B), the secondary flow (B) partially feeds fluid behind the ligament, resulting in one leg of the vortex pair (see detailed underlying mechanisms documented in [27]). Similarly, the spiral primary flow also feeds fluid behind

the same ligament, causing the other leg of the vortex pair. This leg then turns into a longitudinal vortex and is mixed into the spiral primary flow. It is believed that the complex flow mixing observed in the present X-type lattice is caused by the interaction amongst all the aforementioned secondary flows and spiral primary flow.

It should be mentioned that, for clarity, Figs. 8 and 9 only present fluid flow behaviors in an array of half unit cells, which may not be favorable for comprehensive understanding of the overall performance. Therefore, Fig. 10 schematically summarizes the primary and secondary flows in two arrays of complete unit cells. First, two counter-rotating spiral primary flows exist in an array of complete unit cells. Second, both secondary flows (A) and (B) form adjacent to each endwall, with (A) skewed towards the adjacent endwall in contrast to (B). Lastly, secondary flow (C), i.e., two counter-rotating vortices, is present behind every ligament.

4.2.2. Endwall flow pattern and heat transfer

The primary and secondary flows and their interaction result in partial heat dissipation from the substrate, dominated by shear stress on the endwall. To understand this better, Fig. 11(a) displays the visualized endwall flow pattern, showing several high shear regions as indicated by less residual fluorescent powders. The mechanisms underlying the formation of the observed flow pattern are schematically summarized in Fig. 11(b) to facilitate further elaboration.

As shown in Fig. 11, a crescent high shear region in front of two neighboring vertexes is caused by a stronger acceleration of two neighboring spiral primary flows due to blockage by these vertexes. Two additional high shear regions (A) and (B) also exist, which dominate the endwall flow pattern. The secondary flow (A) and the spiral primary flow are skewed towards region (A), whereas the secondary flow (B) and the spiral primary flow are skewed away from region (B). The velocity vectors in plane 2 shown in Fig. 8(b) provides convincing proof for these fluid flow behaviors. Consequently, the shear stress in region (A) appears to be higher than that in region (B). In addition, the presence of another high shear crescent region behind each vertex is attributed to stronger shear by secondary flow (C) formed behind each ligament.

Fig. 11(c) presents the numerically simulated endwall heat transfer distribution, which corresponds to the endwall flow pattern in Fig. 11(a). The local Nusselt number (Nu) is calculated based on local bulk mean fluid temperature of Eq. (5). Overall, the endwall heat transfer in the first two unit cells exhibits a distribution different from that in the last three unit cells, consistent with the endwall flow pattern shown in Fig. 11(a). Note that the flow and heat transfer in the first two unit cells are affected by the entry region. Corresponding to the high shear regions (A) and (B) in Fig. 11(a), the two regions (A) and (B) marked in Fig. 11(c) dominate endwall heat transfer in each unit cell.

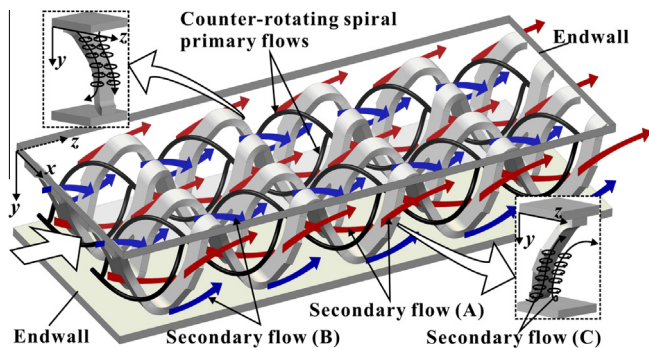


Fig. 10. Summary of primary and secondary flows induced by X-type lattice in two arrays of unit cells.

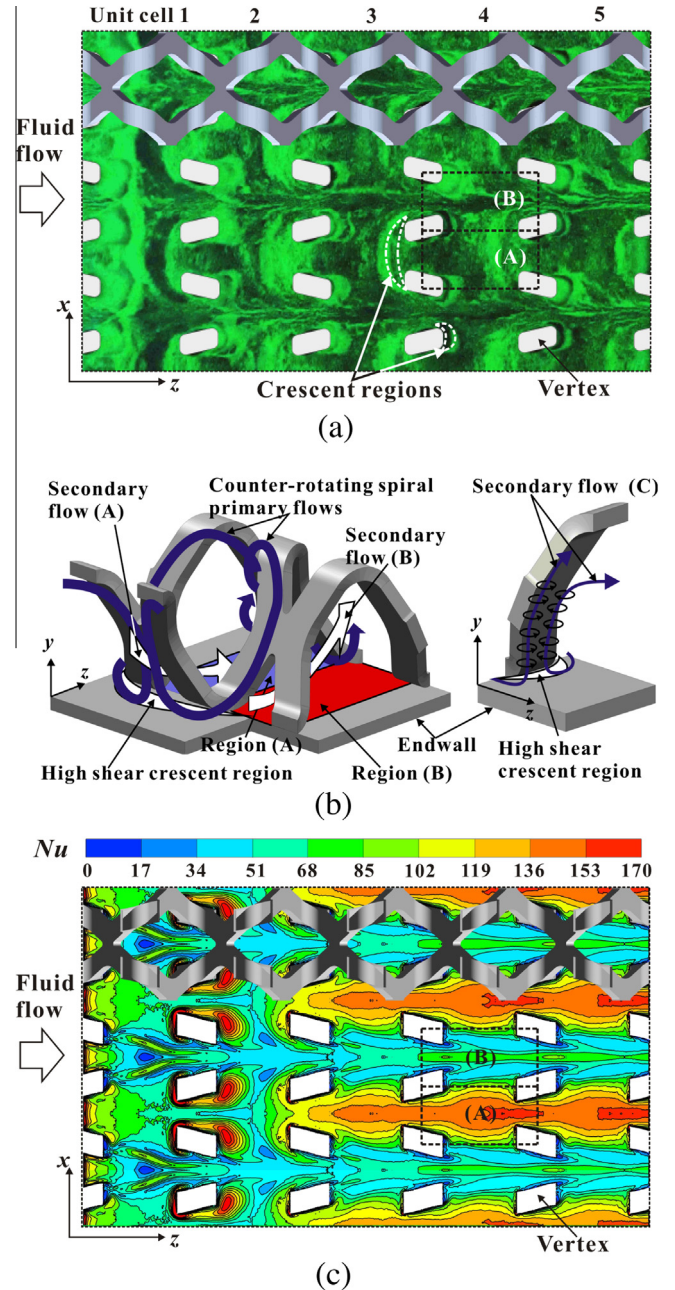


Fig. 11. Endwall flow pattern and corresponding endwall heat transfer: (a) measured endwall flow image; (b) mechanisms underlying the formation of endwall flow pattern; (c) numerically simulated endwall heat transfer distribution at $Re_H = 5700$.

The higher shear stress in region (A) leads to an area-averaged Nusselt number 120% higher than that in region (B), as quantified in Fig. 12. For comparison, the area-averaged Nusselt number on the endwall of a LFM-cored sandwich panel [24] is also plotted in Fig. 12. It is seen that, relative to LFM, a 90% enhancement of endwall heat transfer is achieved by the X-type lattice, which is the first contributor to its substantial overall heat transfer enhancement shown in Fig. 7.

4.2.3. Heat transfer on ligaments

In addition to enhancing substantially the endwall heat transfer, the spiral primary flow and secondary flows also enhance heat transfer on the ligaments of the X-type lattice. Local heat transfer

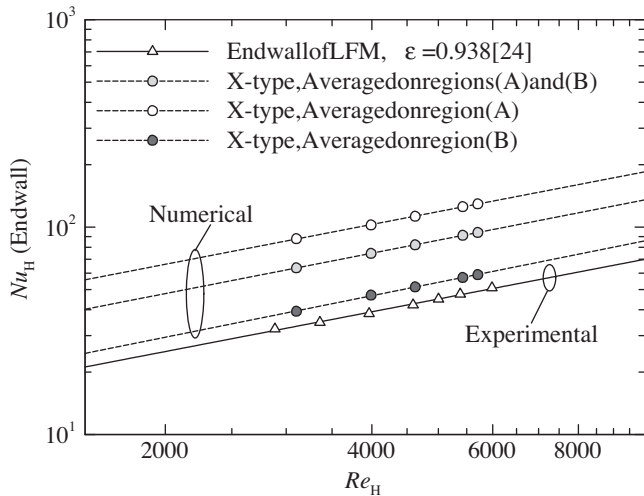


Fig. 12. Comparison of area-averaged Nusselt number on the endwall of fourth unit cell with that on the endwall of LFM-cored sandwich panel [24].

characteristics on these ligaments are shown in Fig. 13 and quantified in Fig. 14 for comprehensive elaboration. The local Nusselt number (Nu) is also based on local bulk mean fluid temperature of Eq. (5).

The surfaces of the X-type lattice ligaments may be divided into five different types, i.e., upstream surface, downstream surface, and surfaces (I)–(III) indicated in Fig. 13. These surfaces experience different fluid flow behaviors, as explained below. First, strong shear by the spiral primary flow causes the highest area-averaged Nusselt number on the upstream surface as shown in Fig. 14. Second, secondary flows (A) and (B) are responsible for local heat transfer on surfaces (I) and (II), respectively. However, the different skewing of these secondary flows relative to the adjacent endwall decreases shear on surface (I) and increases shear on surface (II). Consequently, it is seen from Fig. 14 that the area-averaged Nusselt number on surface (II) is approximately 40% higher than that on surface (I). Thirdly, although surface (III) also experiences spiral primary flow, its area-averaged Nusselt number is approximately 60% lower than that on the upstream surface. Lastly, heat transfer on the downstream surface is dominated by secondary flow (C), where the area-averaged Nusselt number is also approximately 60% lower than that on the upstream surface.

For comparison, the area-averaged Nusselt number on the ligaments of the LFM lattice obtained by Kim et al. [8] is included in Fig. 14. The Nusselt number for LFM is approximated in [8] by modifying the correlation for staggered tube bundles [25], and may finally be expressed as:

$$Nu_H = 1.3919 Re_H^{0.5} \quad (3000 < Re_H < 6000) \quad (10)$$

From the results shown in Fig. 14, it may be concluded that the area-averaged Nusselt number on the ligaments of the X-type lattice is up to 20% higher than that of LFM. Further, the present X-type lattice has a 66% higher surface area density than LFM for a fixed porosity. These two factors act as the second contributor to the substantial overall heat transfer enhancement achieved by the X-type lattice over other PCMs; see Fig. 7.

4.2.4. Summary of heat transfer mechanisms

Fig. 15 summarizes the contributions of the identified heat transfer mechanisms that underlie the forced convective performance of the present X-type lattice sandwich panel. The contributions of regions (A) and (B) in Fig. 11(c) to endwall heat transfer are

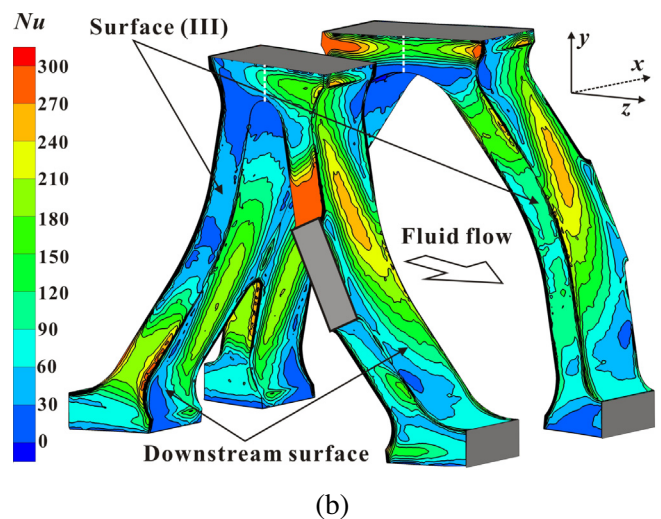
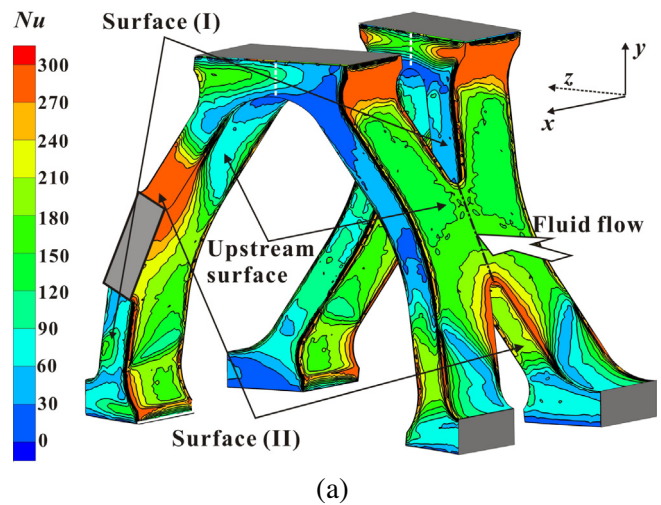


Fig. 13. Simulated heat transfer distribution on X-type lattice ligaments (fourth unit cell, $Re_H = 5700$) viewed from: (a) upstream and (b) downstream.

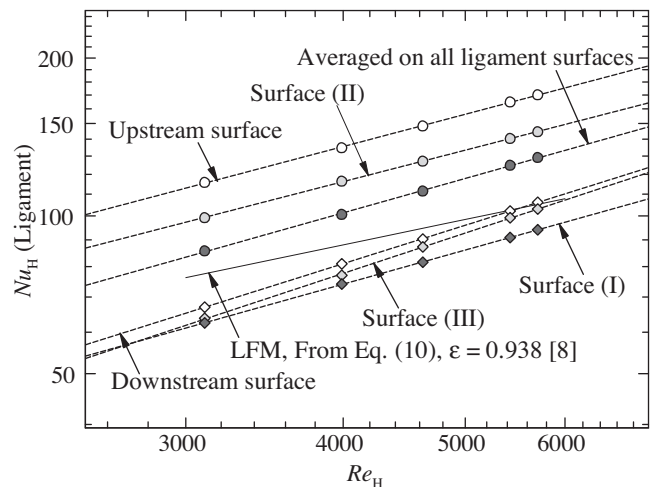


Fig. 14. Comparison of area-averaged Nusselt number on ligament surfaces of fourth unit cell in Fig. 13 with that on ligament surfaces of a LFM lattice core [8].

presented in Fig. 15(a). With region (A) of the fourth unit cell taken as an example, the percentage is calculated as:

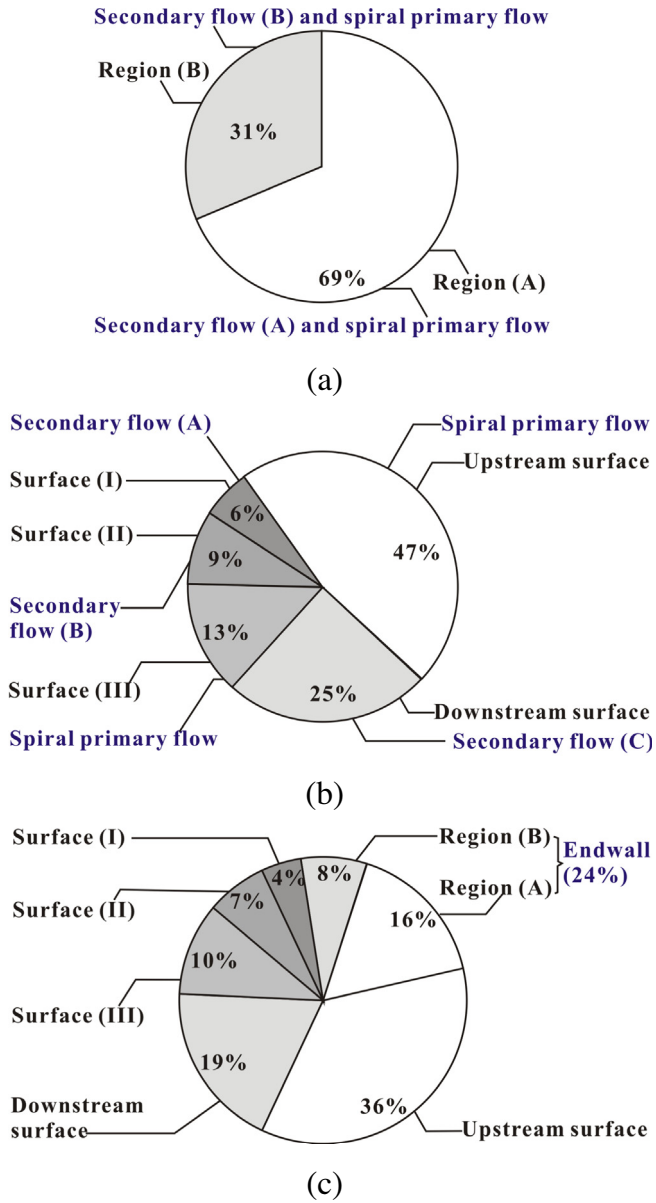


Fig. 15. Summary of contributions of different mechanisms to (a) endwall heat transfer, (b) heat transfer on ligaments and (c) overall heat transfer corresponding to the fourth unit cell.

$$\frac{Nu_{H,region(A)}A_{region(A)}}{Nu_{H,endwall}A_{endwall}} = \frac{\int_{A_{region(A)}} NudA}{\int_{A_{endwall}} NudA} = 69\% \quad (11)$$

where $A_{region(A)}$ and $A_{endwall}$ are the areas of region (A) and the whole endwall surface, respectively; $Nu_{H,region(A)}$ and $Nu_{H,endwall}$ refer to the area-averaged Nusselt number on region (A) and the whole endwall, respectively. It is seen that 69% of the heat is dissipated from region (A), attributing to the secondary flow (A) and the spiral primary flow.

Fig. 15(b) summarizes the contributions of local heat transfer from five different surface types to the heat removal from ligaments, where the percentage is calculated as (take the upstream surface as an example):

$$\frac{Nu_{H,upstream}A_{upstream}}{Nu_{H,ligament}A_{ligament}} = \frac{\int_{A_{upstream}} NudA}{\int_{A_{ligament}} NudA} = 47\% \quad (12)$$

where $A_{upstream}$ and $A_{ligament}$ represent the area of the upstream surface and all the ligament surfaces, respectively. It can be concluded that heat transfer from the upstream and downstream surfaces dissipates 72% of the heat from the ligaments, attributing mainly to the spiral primary flow and the secondary flow (C).

Fig. 15(c) presents a breakdown of the above-mentioned distinctive mechanisms to the overall heat transfer of the X-type lattice sandwich panel, where the percentage is evaluated as (take the upstream surface as an example):

$$\frac{Nu_{H,upstream}A_{upstream}}{Nu_{H,total}A_{total}} = \frac{\int_{A_{upstream}} NudA}{\int_{A_{total}} NudA} = 36\% \quad (13)$$

Here, A_{total} is the total surface area of the heated endwall and ligaments, and $Nu_{H,total}$ is the mean Nusselt number averaged over all these surfaces. It can be concluded that the endwall and ligaments contribute up to 24% and 76% to the overall heat transfer, respectively.

4.3. Pressure drop

Next, pressure drop induced by the X-type lattice is quantified and compared to that caused by LFM and Kagome. Fig. 16(a) plots the pressure drop per unit length along the flow direction ($\Delta P/L$) as a function of mean inlet mean velocity (U_m). Predictions from the present numerical simulation are also included. The pressure drop increases monotonically with increasing flow velocity, exhibiting a quadratic dependence.

The pressure drop results of Fig. 16(a) are re-plotted in Fig. 16(b) in a non-dimensional form, with the friction factor f_H defined in Eq. (7). For reference, the friction factors obtained previously for LFM [4] and Kagome [5] are also included. For the LFM, the flow is laminar when $Re_H < 1963$; transition from laminar to turbulent flow occurs when $1963 < Re_H < 2960$; and the flow becomes turbulent when $Re_H > 2960$, with an approximately constant friction factor of 0.62. For the Kagome, the flow is dominantly turbulent, showing an approximately constant friction factor of 0.56.

For the X-type lattice within the present Reynolds number range ($1400 < Re_H < 7500$), the friction factor is largely independent of the Reynolds number, achieving an approximately constant value of 2.58. Therefore, the pressure drop is dominated by form drag. The X-type lattice causes 3.2 and 3.6 times higher pressure drop than the LFM and Kagome, respectively. Such higher pressure drop is resulted from the complex flow mixing by the interaction among the largely separated primary and secondary flows. The present numerical simulation data exhibit a deviation ranging from 4.4% to 9.3% from the experimental data, which is acceptable.

4.4. Overall thermal performance

For fixed thermal conductivity, porosity and Reynolds number (i.e., coolant mass flow rate), it has been demonstrated that the X-type lattice provides substantially higher overall heat transfer but simultaneously causes higher pressure drop than LFM and Kagome. Therefore, it is necessary to compare thermal efficiency (i.e., heat transfer rate per pumping power) of the X-type lattice to those of other PCMs as a comprehensive evaluation.

For a heat exchanger such as a lattice cored sandwich panel, heat transfer rate is proportional to the Nusselt number (Nu_H), whilst the pumping power required to transport coolant through the lattice core is proportional to $f_H Re_H^3$ [28]. Consequently, a higher value of $Nu_H/(f_H Re_H^3)$ implies higher thermal efficiency. Fig. 17 presents the variation of Nusselt number as a function of non-dimensional pumping power obtained according to Figs. 7(c) and 16(b). At a fixed pumping power within the numerically simulated range,

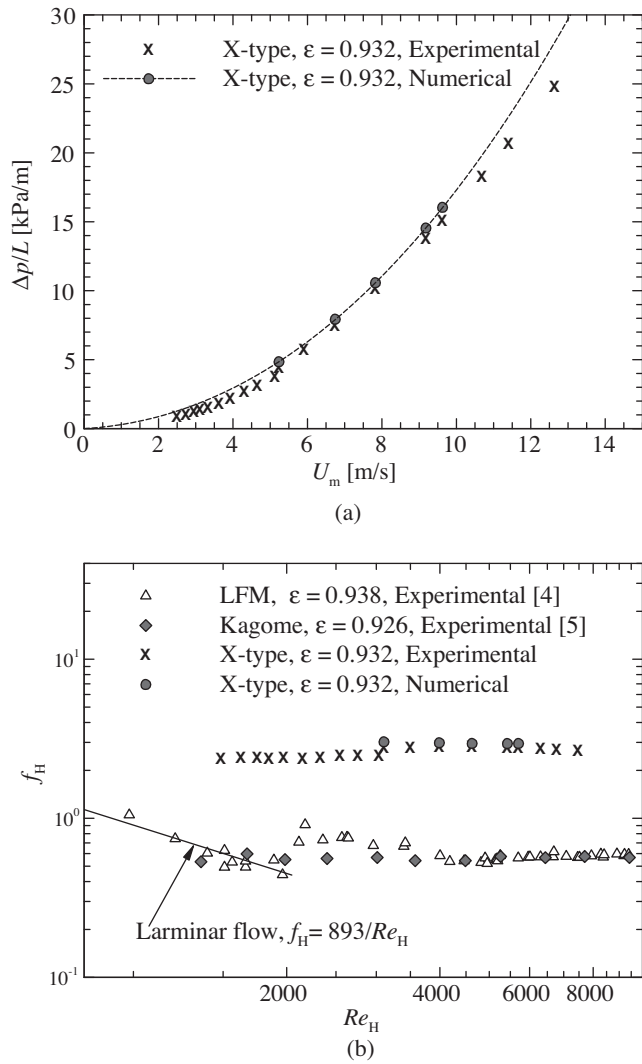


Fig. 16. Pressure drop induced by X-type lattice: (a) $\Delta p/L$ versus U_m ; (b) friction factor versus Reynolds number and comparison to LFM [4] and Kagome [5].

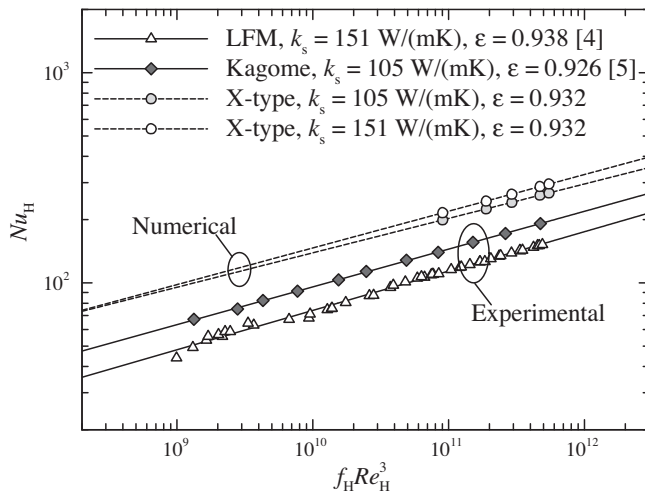


Fig. 17. Thermal performance comparison between X-type lattice and reference PCMs (i.e., LFM [4] and Kagome [5]) under fixed pumping power condition.

Fig. 14 reveals that the present X-type lattice exhibits 89–93% and 36–40% higher heat transfer than LFM and Kagome, respectively.

Hence, better thermal efficiency is achieved by the present X-type lattice under fixed pumping power condition.

5. Conclusions

Focusing on applications requiring simultaneous heat dissipation and mechanical load bearing, this study presents further enhanced convective heat transfer by a newly developed X-type lattice, with direct comparison to other periodic cellular materials. Combined experimental and numerical results provide comprehensive thermo-fluidic behaviors, revealing the underlying mechanisms for heat transfer enhancement. Conclusions drawn in this study are summarized as follows.

- (1) With identical material thermal conductivity and fixed porosity, substantial (up to 170% and 100%) overall heat transfer enhancement can be achieved by the X-type lattice compared to LFM and Kagome, respectively.
- (2) The unique morphology of the X-type lattice induces a highly tortuous spiral primary flow and three different types of secondary flows (i.e., two types of cross flows and a vortex pair). These fluid flow behaviors result in up to 90% and 20% higher area-averaged Nusselt number on the endwall and cell ligaments than that of the LFM. Additionally, higher core surface area density is achieved by the X-type lattice for a fixed porosity. These factors are responsible for the observed substantial overall heat transfer enhancement.
- (3) Comprehensive fluid flow and local heat transfer mechanisms are presented, valuable for other similar studies.
- (4) Complex flow mixing between the global primary flow and local secondary flows in the X-type lattice leads to approximately 3.2 and 3.6 times more pressure drop penalties relative to the LFM and Kagome, respectively.
- (5) For a fixed pumping power, higher heat transfer and thermal efficiency are achieved by the X-type lattice compared to LFM and Kagome.

Conflict of interest

None declared.

Acknowledgments

This research was supported by the National Basic Research Program of China (Grant No.: 2011CB610305) and the National 111 Project of China (Grant No.: B06024).

Appendix A. Calculation of geometric parameters of X-type lattice

The widths (b_1, b_2) of the intersection point shown in Fig. 4(c) can be calculated as:

$$b_1 = w_1 / \cos \frac{\beta}{2} - \frac{l_1}{2} \tan \frac{\beta}{2} + \frac{w}{2} + 2 \left(1 / \cos \frac{\beta}{2} - 1 \right) r_2 \quad (\text{A.1})$$

$$b_2 = \left[\tan \frac{\beta}{2} / \cos \frac{\beta}{2} + 2 / \sin \frac{\beta}{2} - 1 / \left(\sin \frac{\beta}{2} \cos^2 \frac{\beta}{2} \right) \right] w_1 + 2 \left(1 / \sin \frac{\beta}{2} - 1 \right) r_1 + \left[1 / \left(2 \cos^2 \frac{\beta}{2} \right) - \tan^2 \frac{\beta}{2} / 2 \right] l_1 + \left[\tan \frac{\beta}{2} / 2 - 1 / \left(2 \sin \frac{\beta}{2} \cos \frac{\beta}{2} \right) \right] w \quad (\text{A.2})$$

The fillet radius r_3 shown in Fig. 4(e) can be calculated as:

$$r_3 = l \cos \frac{\alpha}{2} / \left[4 \left(1 - \sin \frac{\alpha}{2} \right) \right] + t_1 \left(\sin \frac{\alpha}{2} - \frac{1}{2} \right) / \left(1 - \sin \frac{\alpha}{2} \right) - H \sin \frac{\alpha}{2} / \left[2 \left(1 - \sin \frac{\alpha}{2} \right) \right] \quad (\text{A.3})$$

The porosity (ε) of the X-type lattice is given by:

$$\varepsilon = 1 - \frac{t_1}{lWH} \left[wl_1 - 4 \left(\frac{w-b_1}{2} + r_2 / \cos \frac{\beta}{2} - r_2 \right) \times \left(\frac{l_1-b_2}{2} + r_1 / \sin \frac{\beta}{2} - r_1 \right) + 4 \left(\cot \frac{\beta}{2} - \frac{\pi-\beta}{2} \right) r_1^2 + 4 \left(\tan \frac{\beta}{2} - \frac{\beta}{2} \right) r_2^2 \right] \quad (\text{A.4})$$

The surface area density (ρ_{SA}) of the X-type lattice is calculated as:

$$\rho_{SA} = \frac{2(1-\varepsilon)}{t_1} + \frac{8t_1}{lWH} \left\{ \left(1 / \sin \frac{\beta}{2} \right) \left[\frac{w}{4} - w_1 / \left(2 \cos \frac{\beta}{2} \right) + \frac{l_1}{4} \tan \frac{\beta}{2} \right] + \left(\frac{\pi-\beta}{2} - \cot \frac{\beta}{2} \right) r_1 + \left(\frac{\beta}{2} - \tan \frac{\beta}{2} \right) r_2 \right\} \quad (\text{A.5})$$

In the above equations, l_1 is obtained as:

$$l_1 = l / \sin \frac{\alpha}{2} + \left(2\pi - 2\alpha - 4 \cot \frac{\alpha}{2} \right) r_3 + \left(\pi - \alpha - 2 \cot \frac{\alpha}{2} \right) t_1 \quad (\text{A.6})$$

References

- [1] J. Armstrong, D. Winstanley, A review of staggered array pin fin heat transfer for turbine cooling applications, *ASME J. Turbomach.* 110 (1) (1988) 94–103.
- [2] K. Boomsma, D. Poulikakos, F. Zwick, Metal foams as compact high performance heat exchangers, *Mech. Mater.* 35 (12) (2003) 1161–1176.
- [3] J. Tian, T.J. Lu, H.P. Hodson, D.T. Queheillalt, H.N.G. Wadley, Cross flow heat exchange of textile cellular metal core sandwich panels, *Int. J. Heat Mass Transfer* 50 (13) (2007) 2521–2536.
- [4] T. Kim, H.P. Hodson, T.J. Lu, Pressure loss and heat transfer mechanisms in a lattice-frame structured heat exchanger, *IMEchE J. Mech. Eng. Sci.* 218 (11) (2004) 1321–1336.
- [5] F. Hoffmann, Heat transfer performance and pressure drop of Kagome core metal truss panels, Master thesis, University of Cambridge, Cambridge, UK, 2002.
- [6] J.F. Rakow, A.M. Waas, Thermal bucking of metal foam sandwich panels for convective thermal protection systems, *J. Spacecraft Rockets* 42 (5) (2005) 832–844.
- [7] J.F. Rakow, A.M. Waas, Response of actively cooled metal foam sandwich panels exposed to thermal loading, *AIAA J.* 45 (2) (2007) 329–336.
- [8] T. Kim, C.Y. Zhao, T.J. Lu, H.P. Hodson, Convective heat dissipation with lattice-frame materials, *Mech. Mater.* 36 (8) (2004) 767–780.
- [9] S.S. Feng, M.Z. Li, J.H. Joo, K.J. Kang, T. Kim, T.J. Lu, Thermomechanical properties of brazed wire-woven bulk Kagome cellular metals for multifunctional applications, *J. Thermophys. Heat Transfer* 26 (1) (2012) 66–74.
- [10] H.B. Yan, Q.C. Zhang, T.J. Lu, An X-type lattice cored ventilated brake disc with enhanced cooling performance, *Int. J. Heat Mass Transfer* 80 (2015) 458–468.
- [11] H.N.G. Wadley, Multifunctional periodic cellular metals, *Philos. Trans. R. Soc. A* 364 (1838) (2006) 31–68.
- [12] Y.-H. Lee, B.-K. Lee, I. Jeon, K.-J. Kang, Wire-woven bulk Kagome truss cores, *Acta Mater.* 55 (18) (2007) 6084–6094.
- [13] V.S. Deshpande, N.A. Fleck, M.F. Ashby, Effective properties of the octet-truss lattice material, *J. Mech. Phys. Solids* 49 (8) (2001) 1747–1769.
- [14] D.T. Queheillalt, H.N.G. Wadley, Cellular metal lattices with hollow trusses, *Acta Mater.* 53 (2) (2005) 303–313.
- [15] H.N.G. Wadley, N.A. Fleck, A.G. Evans, Fabrication and structural performance of periodic cellular metal sandwich structures, *Comput. Sci. Technol.* 63 (16) (2003) 2331–2343.
- [16] G.W. Kooistra, H.N.G. Wadley, Lattice truss structures from expanded metal sheet, *Mater. Des.* 28 (2) (2007) 507–514.
- [17] Q.C. Zhang, Y.J. Han, C.Q. Chen, T.J. Lu, Ultralight X-type lattice sandwich structure (I): concept, fabrication and experimental characterization, *Sci. China Ser. E: Tech. Sci.* 52 (8) (2009) 2147–2154.
- [18] Q.C. Zhang, A.P. Chen, C.Q. Chen, T.J. Lu, Ultralight X-type lattice sandwich structure (II): micromechanics modeling and finite element analysis, *Sci. China Ser. E: Tech. Sci.* 52 (9) (2009) 2670–2680.
- [19] J.-H. Joo, K.-J. Kang, T. Kim, T.J. Lu, Forced convective heat transfer in all metallic wire-woven bulk Kagome sandwich panels, *Int. J. Heat Mass Transfer* 54 (25) (2011) 5658–5662.
- [20] T. Wen, J. Tian, T.J. Lu, D.T. Queheillalt, H.N.G. Wadley, Forced convection in metallic honeycomb structures, *Int. J. Heat Mass Transfer* 49 (19) (2006) 3313–3324.
- [21] H.W. Coleman, W.G. Steele, *Experimentation, Validation, and Uncertainty Analysis for Engineers*, third ed., John Wiley & Sons Inc., Hoboken, New Jersey, 2009.
- [22] F.R. Menter, Two-equation eddy-viscosity turbulence models for engineering applications, *AIAA J.* 32 (8) (1994) 1598–1605.
- [23] F.R. Menter, M. Kuntz, R. Langtry, Ten years of industrial experience with the SST turbulence model, in: K. Hanjalić, Y. Nagano, M. Tummers (Eds.), *Turbulence Heat and Mass Transfer*, vol. 4, Begell House Inc., Danbury, USA, 2003, pp. 625–632.
- [24] T. Kim, H.P. Hodson, T.J. Lu, Fluid-flow and endwall heat-transfer characteristics of an ultralight lattice-frame material, *Int. J. Heat Mass Transfer* 47 (6) (2004) 1129–1140.
- [25] A. Žukauskas, Heat transfer from tubes in crossflow, in: J.P. Hartnett, T.F. Irvine (Eds.), *Advances in Heat Transfer*, vol. 18, Academic Press Inc., Orlando, USA, 1987, pp. 87–159.
- [26] T. Kim, H.P. Hodson, T.J. Lu, Contribution of vortex structures and flow separation to local and overall pressure and heat transfer characteristics in an ultralightweight lattice material, *Int. J. Heat Mass Transfer* 48 (19) (2005) 4243–4264.
- [27] I.K. Choi, T. Kim, S.J. Song, T.J. Lu, Endwall heat transfer and fluid flow around an inclined short cylinder, *Int. J. Heat Mass Transfer* 50 (5) (2007) 919–930.
- [28] J. Tian, T. Kim, T.J. Lu, H.P. Hodson, D.T. Queheillalt, D.J. Sypeck, H.N.G. Wadley, The effects of topology upon fluid-flow and heat-transfer within cellular copper structures, *Int. J. Heat Mass Transfer* 47 (14) (2004) 3171–3186.